Research Square

Preprints are preliminary reports that have not undergone peer review.
They should not be considered conclusive, used to inform clinical practice,
or referenced by the media as validated information.

Programmable Terahertz Waveform Synthesis via Coherent Interference of Phonon Polaritons

Ye Tian

tianye@siom.ac.cn

Shanghai Institute of Optics and Fine Mechanics, Chinese Academy of Sciences
https://orcid.org/0000-0002-5618-5951

Jixing Gao

Shanghai Institute of Optics and Fine Mechanics https://orcid.org/0009-0005-1219-1910

Jiajing Hao

Shanghai Institute of Optics and Fine Mechanics https://orcid.org/0009-0004-1862-7255

Yifei Fang

Shanghai Institute of Optics and Fine Mechanics

Liwei Song

Shanghai Institute of Optics and Fine Mechanics https://orcid.org/0000-0002-0538-3472

Ruxin Li

Shanghai Institute of Optics and Fine Mechanics https://orcid.org/0000-0002-2603-9814

Article

Keywords:

Posted Date: April 29th, 2026

DOI: https://doi.org/10.21203/rs.3.rs-9092994/v1

License: This work is licensed under a Creative Commons Attribution 4.0 International License.
Read Full License

Additional Declarations: There is no conflict of interest

Programmable Terahertz Waveform Synthesis via Coherent Interference of Phonon Polaritons

JIXING GAO,[1,2] JIAJING HAO,[1,2] YIFEI FANG,[1,2,*] LIWEI SONG,[1,2,*] YE TIAN,[1,2,*] AND RUXIN LI,[1,2,3]

[1]*State Key Laboratory of Ultra-intense laser Science and Technology, Shanghai Institute of Optics and Fine Mechanics, Chinese Academy of Sciences, 201800 Shanghai, China*

[2]*Center of Materials Science and Optoelectronics Engineering, University of Chinese Academy of Sciences, 100049 Beijing, China*

[3]*Zhangjiang Laboratory, Shanghai 201210, China*

These authors contributed equally: Jixing Gao, Jiajing Hao

**Corresponding author: yifeifang@siom.ac.cn; slw@siom.ac.cn; tianye@siom.ac.cn*

Abstract: Terahertz photonics lacks a flexible platform for synthesizing arbitrary coherent waveforms, limiting applications in ultrafast control and quantum information. Here we introduce a phase-matching-directed nonlinear synthesis scheme that transforms the four-wave mixing detection process into a programmable waveform generator. Using intense terahertz pulses to excite broadband phonon polaritons in α-quartz, the phase-matching condition actively selects two specific polariton frequencies. Their coherent interference, mediated by third-order nonlinearity, produces an optical beat note at their difference frequency—a virtual frequency that is not constrained by material eigenmodes but is dictated by externally imposed parameters. This allows us to synthesize beat frequencies of 4.3/6.0 THz (extraordinary branch) and 6.3/7.1 THz (ordinary branch) in the optical signal. Furthermore, we introduce a double-terahertz-pulse excitation scheme that decomposes the broadband pump into two narrowband pulses aligned with the selected polariton modes. By independently tuning their carrier-

envelope phases and field strengths, we achieve decoupled control over the temporal waveform and modulation depth of the synthesized beat note while keeping the beat frequency constant. This work establishes a universal framework for all-optical engineering of coherent terahertz waveforms, applicable to a wide range of dielectrics and scalable to other frequency domains. It paves the way for programmable terahertz photonic devices and coherent control of quantum systems.

Introduction

Phonon polaritons (PhPs), hybrid quasiparticles arising from the strong coupling between photons and transverse optical phonons in polar crystals, have emerged as a core platform for optical manipulation in the terahertz (THz)-frequency range[1-7]. Their ability to confine electromagnetic fields at subwavelength scales[8] and enhance light-matter interactions[9] has driven extensive research. Thus, achieving precise and dynamic control over their excitation and propagation is a critical challenge for unlocking their potential in next-generation THz photonic devices[10,11], information processing[12], and energy technologies[13].

Current strategies for PhPs modulation are systematically developed along three dimensions[7,14]: material engineering (e.g., anisotropic van der Waals materials[3,6,14], hexagonal boron nitride[9,15-17], phase-change materials[18,19]), external-stimulation(e.g., electrostatic gating[9,10,20,21], intense THz pulse[16,22-26]), structural-design(e.g., metasurfaces[27], periodic structures[28] and nanoantennas[29]). These advances have collectively promoted the exploration of PhPs in applications such as high-resolution imaging[19], nanoscale photothermal management[13] and integrated on-chip photonic circuits[14].

Despite these notable successes, existing schemes face fundamental limitations. First, most approaches[7,14,30] are static or quasi-static, lacking the flexibility for reconfiguration, especially on ultrafast timescales. Second, external-field-based modulation[10] often depends on specific intrinsic materials parameters (e.g., carrier mobility[21], anharmonic coupling

coefficients[24]), limiting generality. More importantly, the prevailing perspective treats the PhPs system as a passive responder. Conventional methods, whether observing unique propagation modes[8,31,32] or inducing novel states of matter[18,19], essentially excite the material's intrinsic modes and observe the ensuing dynamics dictated by the material's dispersion. For example, the beat notes observed in ferroelectrics such as $LiTaO_3$[33] or $LiNbO_3$[34] are interpreted as static spectral fingerprints from the interference of two eigenmodes at a fixed wavevector. Even advanced techniques like wavevector-selective four-wave-mixing (FWM)[35], typically address only a single wavevector (and thus a single frequency) at a time, generating or controlling beat notes. This is a significant constraint: beat frequency provide crucial insights into coupling strength and Rabi splitting[9,27,36,37], the current material-centric paradigm confines functionality to fixed resonance windows and hinders the on-demand synthesis of dynamic optical fields.

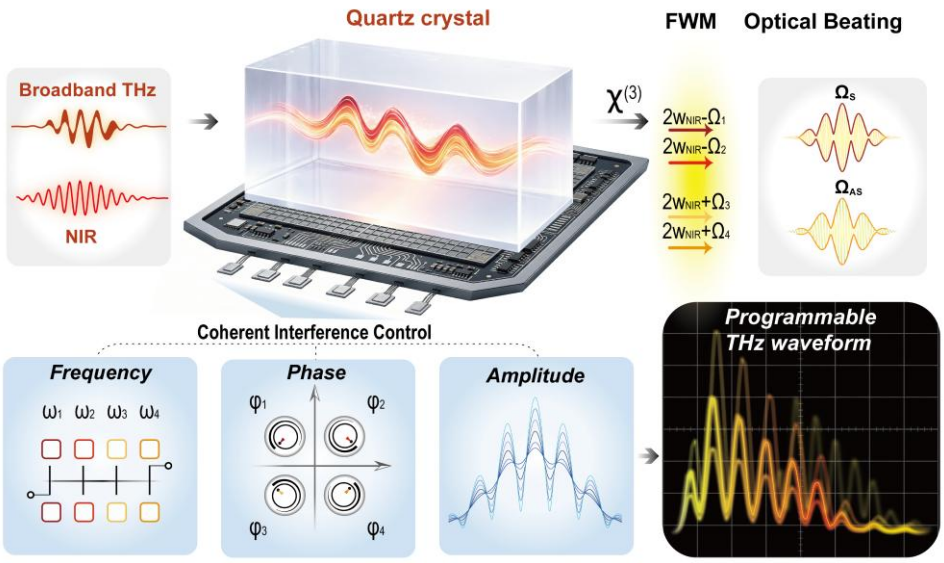


Fig. 1 Programmable Terahertz Waveform Synthesis. Bulk PhPs are generated in SiO_2 by coupling phonons with intense, broadband, and frequency-tunable THz pulses. During their forward propagation, a collinear near-infrared probe pulse, through phase matching, selectively generates two specific-frequency PhPs in both the Stokes and anti-Stokes processes. The two PhPs from the same process then interfere via third-

order nonlinearity, producing a coherent beat note at a frequency equal to their difference. For instance, with THz polarization along the ΓA direction, Ω_{AS} and Ω_{S} correspond to 4.3 THz and 6.0 THz, respectively. Consequently, the time-domain FWM signal manifests as a picosecond oscillatory decay at the frequency $\Omega_{AS/S}$.

Here we transcend this limitation by introducing a paradigm shift (Fig. 1): instead of observing material-intrinsic beats, we actively synthesize virtual beat frequencies in the optical domain—frequencies that are not native to the material but emerge as the difference between two phase-matched phonon polaritons. This 'virtual frequency' is entirely determined by our experimental design (phase-matching condition and probe wavelength) and can be tuned independently of material eigenmodes. Using intense THz pulses to excite broadband PhP dispersion in α-quartz, we employ a collinear near-infrared (NIR) probe geometry where the detection process is strictly governed by the phase-matching condition of third-order nonlinear four-wave mixing. This condition acts as an active frequency selector, picking two specific components from the broadband spectrum. Their subsequent coherent interference generates a distinct beat note in the time-domain FWM signal. Crucially, we demonstrate that this beat note is not a material fingerprint but a synthetic product co-determined by the material dispersion and externally imposed phase-matching conditions, which can be flexibly adjusted by experimental geometry. Furthermore, we introduce a double-THz-pulse coherent excitation scheme that achieves decoupled, multi-parameter control over the synthesized waveform—independently tuning the temporal shape and modulation depth while keeping the beat frequency constant. This establishes a universal framework for all-optical engineering of coherent terahertz waveforms, transforming nonlinear optical detection from a spectroscopic probe into an active synthesis platform.

Results

PhP Dynamics in Crystalline SiO_2

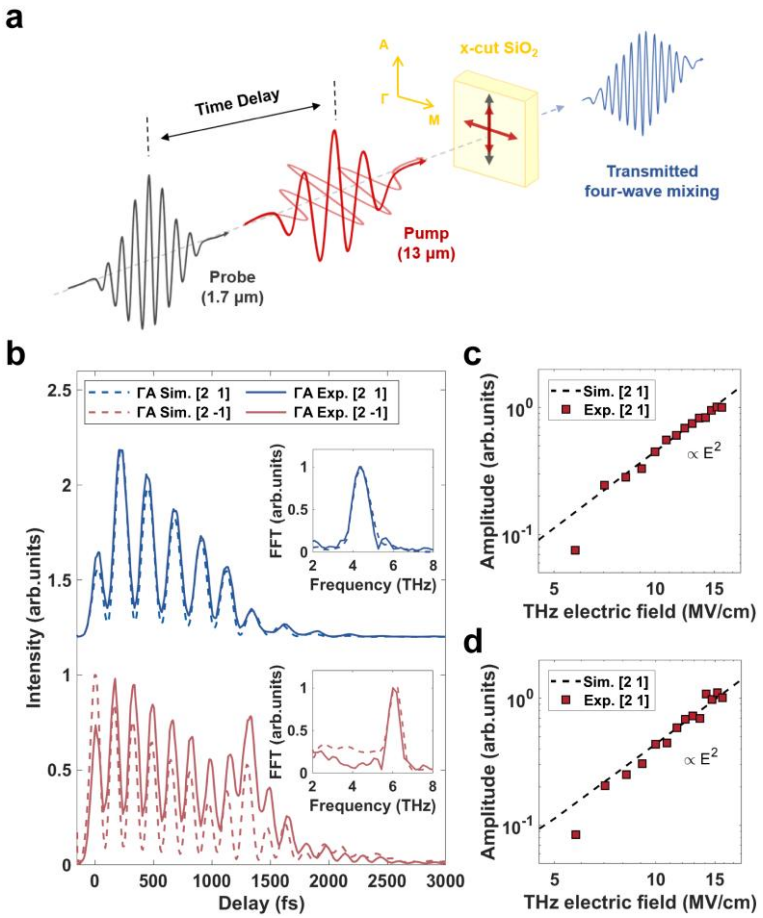


Fig. 2 Time-resolved FWM dynamics of PhPs in SiO_2. a Schematic of the experimental setup. The probe and pump pulses are centered at 1.7 μm and 13 μm (23 THz), respectively. **b** Time-resolved FWM signal as a function of pump-probe delay, with the pump polarized along ΓA direction. The left inner panel is the fourier transform of the time-delay trace. **c, d** Scaling law of THz field strength. The solid lines (with solid symbols) and dashed lines represent experimental and simulated results, respectively. The notations "[2 1]" and "[2 -1]" correspond to the high-energy and low-energy FWM photon signals, respectively, and are used consistently throughout this work.

As shown in Fig. 2a, an intense THz pulse was focused onto an x-cut SiO_2 crystal with its polarization aligned along the ΓA or ΓM direction. This configuration directly excited the corresponding A_2- or E-symmetry infrared-active phonon modes, and launched extraordinary

or ordinary PhPs, respectively. The polarization of NIR probe pulse was fixed along the ΓA direction to suppress contributions from second-order nonlinearities. Transmitted probe spectra under different polarization configurations were recorded with a spectrometer. In the time-resolved FWM measurements, picosecond-scale oscillations were observed and are labeled as [m n], corresponding to a photon energy of $m\omega_{\mathrm{NIR}} + n\omega_{\mathrm{PhP}}$. As shown in Fig. 2b, [2 1] signal persisted for ~2 ps and oscillated at 4.3(±0.3) THz, whereas the [2 -1] signal lasted ~3 ps with an oscillation frequency of 6.0(±0.3) THz. The [2 1] signal is approximately one order of magnitude stronger than [2 -1] signal (Supplementary Fig. S1). Varying the THz pump amplitude further revealed that the Fourier amplitude of the low-frequency component scales quadratically with the THz electric field amplitude (Figs. 2c).

These low-frequency dynamics suggest a well-established mechanism[23,38-41], in which nonlinear phonon rectification can coherently drive a Raman phonon mode and imprint its oscillation onto the optical response at the Raman-mode frequency. We first assess whether a Raman-phonon pathway could account for the observed dynamics. However, the oscillation frequencies differ between the [2 1] and [2 −1] signals, which is not expected for a single Raman mode. These considerations instead point to phase matching as the key ingredient. Using the PhP dispersion and the FWM phase-matching condition, we assign the [2 1] and [2 -1] signals to anti-Stokes and Stokes processes, respectively (see Materials and Methods). Importantly, phase matching selects two PhP frequency components within the bandwidth of the driving THz spectrum, and the observed low-frequency oscillation corresponds to the difference frequency between these two phase-matched PhPs.

To investigate the polarization dependence expected from the phase-matching condition, the THz polarization was rotated from ΓA to ΓM direction (See Supplementary Fig. S2). The oscillation frequencies of the [2 1] and [2 -1] signals are 6.3(±0.3) THz and 7.1(±0.3) THz, respectively. In the analysis, only forward-propagating pathways are considered, corresponding to the dispersion branches indicated by the dashed and solid lines in Supplementary Fig. S3.

Under this constraint, the observed oscillations remain consistent with the beat frequencies expected from the two phase-matched PhP modes. To account for propagation effects and enable quantitative comparison, finite-difference time-domain (FDTD) simulations of THz pulse propagation in α-SiO_2 were performed. For both ΓA and ΓM polarizations, the simulations reproduce the measured temporal oscillations and the low-frequency components of the FWM response (see Materials and Methods).

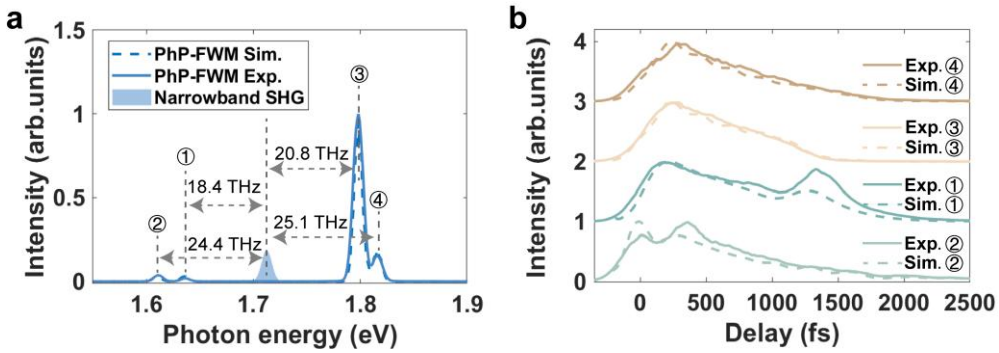


Fig. 3 Phase-matching characteristics of PhPs with a narrowband probe. a Spectrum of the FWM signal at a pump-probe delay of 250 fs, compared with the reference second-harmonic spectrum (color-shaded regions, the angle between the polarization of the probe pulse and the ΓA direction is 20 degrees). The probe spectrum is centered at 1.45 μm with a FWHM bandwidth of 12 nm. Horizontal dashed arrow lines mark the frequencies of the PhPs generated via the FWM process. **b** Corresponding time-domain FWM signals. The numeric labels correspond to the spectral peaks indicated in **a**.

While a broadband probe excites FWM over a wide spectral range, where the two phase-matched PhP branches overlap. This produces a strong beat modulation in the delay-dependent intensity. However, due to its limited spectral resolution, the measured FWM photon energy cannot be reliably traced back to the exact phase-matched PhP frequencies. The NIR probe was spectrally filtered to a 12 nm bandwidth to improve spectral discrimination (Fig. 3). For the forward-propagating anti-Stokes process, the phase-matching condition yields two phase-

matched PhP frequencies at 20.8(±0.3) THz and 25.1(±0.3) THz, which appear as a doublet (peaks 3 and 4) in the 1.75 - 1.85 eV range (Fig. 3a). Correspondingly, for the Stokes process, the phase-matching condition gives rise to frequencies at 18.4(±0.3) THz and 24.4(±0.3) THz, producing a second doublet (peaks 1 and 2) in the 1.58 - 1.68 eV range.

By resolving the response into separate spectral peaks, each peak becomes dominated by a single phase-matched PhP solution. This separation strongly suppresses the beat-note contribution within individual peaks (Fig. 3b), enabling the unambiguous assignment of each FWM peak to its corresponding phase-matched PhP frequency. This direct observation of the two constituent frequencies confirms that the subsequent beat note observed in broadband measurements arises from their coherent interference—a synthesized virtual frequency rather than a native material mode.

Coherent interference of PhPs

To explain the observed low-frequency oscillations and their polarization dependence, we formulate a model for the ultrafast dynamics of PhPs underlying the FWM response. The pump THz field drives the infrared-active lattice polarization of α-SiO_2 and launches propagating PhP wavepackets. Their linear propagation is described by the Huang–Kun formalism coupled with Maxwell's equations, yielding the dispersion relation $k(\omega) = \omega/c\sqrt{\varepsilon(\omega)}$, where the dielectric function $\varepsilon(\omega)$ is given by Eq. (5). Equation (5) is equivalent to a sum of Lorentz oscillators for the IR-active TO modes. In the time domain, the mode-resolved polarization $P_{\mathrm{j}}(t)$ obeys:

$$\frac{d^2P_{\mathrm{j}}}{dt^2} + \gamma_{\mathrm{j}}\frac{dP_{\mathrm{j}}}{dt} + \Omega_{\mathrm{TO-j}}^2 P_{\mathrm{j}} = \epsilon_0 S_{\mathrm{TO-j}}\Omega_{\mathrm{TO-j}}^2 E_{\mathrm{THz}}, \quad \mathrm{j} = 1,2,3,\ldots \tag{1}$$

here, γ_{j} is the damping coefficient, $\Omega_{\mathrm{TO-j}}$ is the TO-mode eigenfrequency, ϵ_0 is the vacuum permittivity, and $S_{\mathrm{TO-j}}$ is the oscillator strength (See Supplementary Table S1). Combining this with nonlinear optics and Maxwell's equations, the nonlinear interaction between the PhP field and the probe can be simulated in the time domain (See Materials and methods).

The mechanism responsible for generating the low-frequency oscillation is the phase-matching constraint inherent to the collinear FWM geometry. For a probe spectrum centered at ω_{NIR}, a quasi-degenerate description is used, in which the two probe photons are taken at the probe center frequency. The generated FWM signals must satisfy energy conservation $\omega_{\mathrm{FWM}} = 2\omega_{\mathrm{NIR}} + s\Omega$ and momentum conservation $k(\omega_{\mathrm{FWM}}) = 2k(\omega_{\mathrm{NIR}}) + sk_{\mathrm{PhP}}(\Omega)$ (See Supplementary Note 5). For a given probe frequency ω_{NIR}, the phase-matching condition intersects the PhP dispersion at two allowed PhP frequencies within the bandwidth of the driving THz spectrum, denoted as Ω_1 and Ω_2 (Fig. 4a). For example, in the [2 -1] process, these correspond to approximately 18.4 THz and 24.4 THz. Crucially, as both components are coherently driven by the same THz pulse, they inherit a well-defined relative phase. The resulting PhP field contains multiple frequencies, but only two components contribute to this FWM process. Thus, the generated FWM field at the selected optical output frequency can be expressed as the coherent sum of the two phase-matched pathways:

$$E_{\mathrm{FWM}}(\tau) = C_1 e^{-\tau/T_1} e^{-i(\Omega_1\tau+\phi_1)} + C_2 e^{-\tau/T_2} e^{-i(\Omega_2\tau+\phi_2)} \quad (2)$$

here, C_i scale with the THz spectral amplitude $|E_{\mathrm{THz}}(\Omega_i)|$ weighted by the coupling and the phase-matching efficiency at Ω_i, T_i denotes the dephasing time of each contribution and ϕ_{i} is the corresponding phase. The detected signal is proportional to the spectral intensity $I_{\mathrm{FWM}}(\tau) \propto |E_{\mathrm{FWM}}(\tau)|^2$, expanding $I_{\mathrm{FWM}}(\tau)$ yields two self-terms and an interference cross-term:

$$I_{\mathrm{FWM}}(\tau) \propto |C_1|^2 e^{-2\tau/T_1} + |C_2|^2 e^{-2\tau/T_2} + 2|C_1||C_2| e^{-\tau/T} \cos\left(\Omega_{AS/S}\tau + \phi_-\right) \quad (3)$$

where $1/T = 1/T_1 + 1/T_2$, $\Omega_{AS/S} = \Omega_1 - \Omega_2$ and $\phi_- = \phi_1 - \phi_2 + \arg C_1 - \arg C_2$. The interference term produces and oscillation at the difference-frequency $\Omega_{\mathrm{AS/S}} = |\Omega_1 - \Omega_2|$, i.e., the beat note between the two phase-matched PhP solutions. Thus, the observed FWM signal in the experiment can be expressed as

$$I_{\mathrm{FWM}}(\tau) = I_0(\tau)\left[1 + \eta(\tau)\cos\left(\Omega_{AS/S}\tau + \phi_-\right)\right] \quad (4)$$

where $\eta(\tau)$ is the modulation depth. Performing a Fourier transform on this time-domain signal yields a peak in the frequency domain centered at $\Omega_{\mathrm{AS/S}}$, with an amplitude scaling

as $|C_1||C_2| \propto |E_{\mathrm{THz}}(\Omega_1)E_{\mathrm{THz}}(\Omega_2)|$, i.e., quadratic in the overall THz field amplitude (details in Supplement), also confirming a $\chi^{(3)}$-mediated interference origin. This formulation reveals that the FWM detection process effectively operates as a waveform synthesizer: the beat frequency is set by the phase-matching condition, while the temporal waveform and modulation depth can be independently programmed via external parameters.

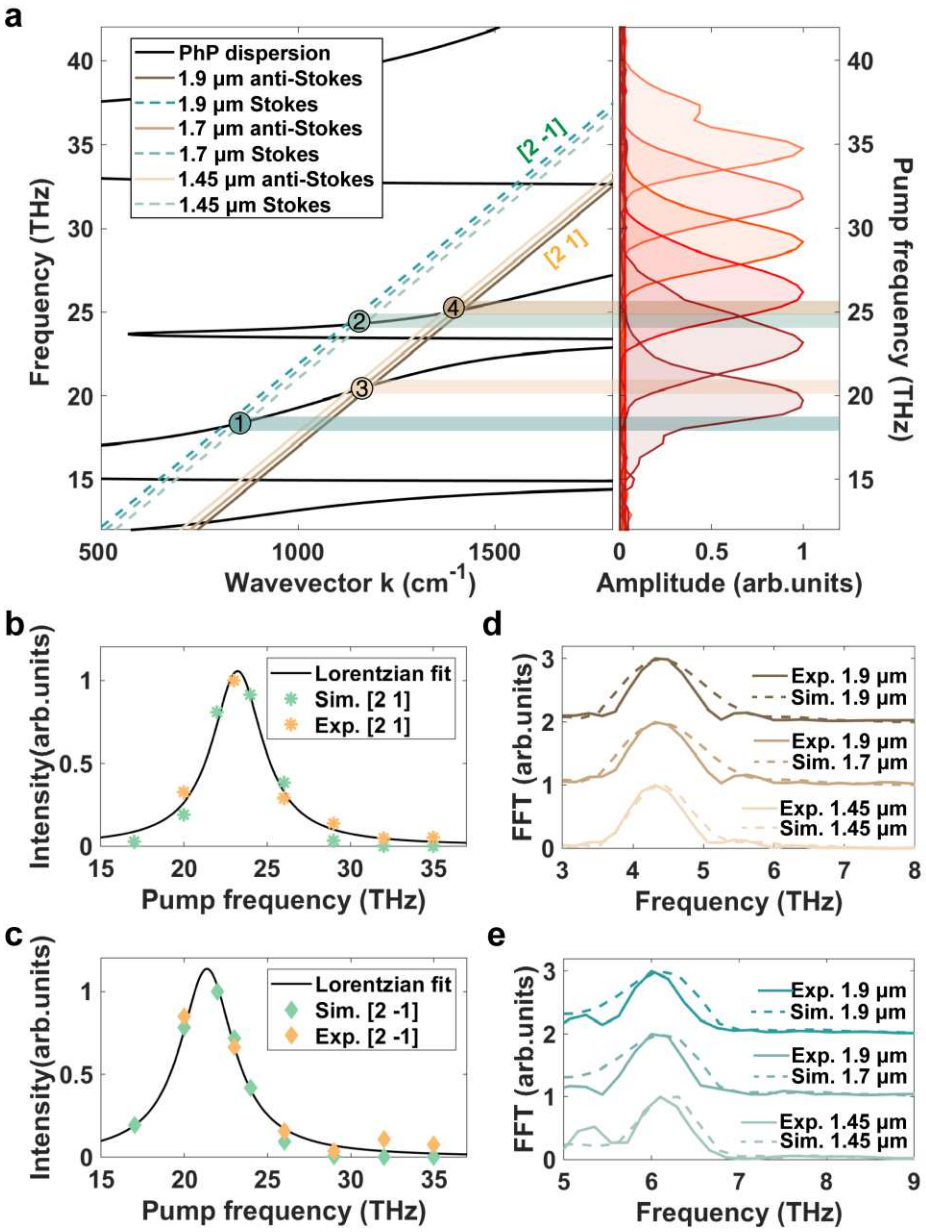


Fig. 4 Dynamic properties of PhPs in quartz crystals. a Dispersion curves of PhPs and phase matching of probe pulses with electric field polarization along ΓA. The different red colors in the right panel represent the THz spectra in **b**, respectively. **b, c** Variation of low-frequency oscillation frequency amplitude in FWM with THz frequency. The black line represents a Lorentzian fit to the simulations, with a full width at half maximum of approximately 3 THz. The green symbols represent data from FDTD simulations, and the yellow symbols represent data from experimental results. **d, e** Fourier-Transform of the FWM signal as a function of probe wavelength. The solid lines and dashed lines represent the experimental and simulated results, respectively.

This model also clarifies the dependence of the modulation strength on the pump spectrum. Because the low-frequency beat arises from two phase-matched PhP components, reducing the THz spectral weight (or phase-matching efficiency) at either Ω_1 or Ω_2 suppresses the modulation amplitude. As shown in Fig. 4a, the THz spectrum (centered around 22-23 THz) covers the phase-matched PhP frequencies selected by the probe. Notably, its overlap with the PhPs involved in the [2 1] process is better than that for the [2 -1] process, which contributes to the order-of-magnitude difference in signal strengths, in addition to differences in phase-matching efficiency. As shown in Fig. 4b and 4c, the experimentally measured integrated oscillation amplitudes and the corresponding calculated values, normalized and plotted as yellow and green symbols respectively, show good agreement across the THz center frequency tuning range of 17 to 35 THz. The simulation results are fitted with a Lorentzian function, yielding a FWHM of ~3 THz for both processes. The maximum oscillation amplitudes for the [2 1] and [2 -1] processes occur at THz center frequencies of approximately 23.5 THz and 21.5 THz, respectively. By selecting NIR probe pulses of different wavelengths (Fig. 4d, e), different PhPs frequencies can be phase-matched. This behavior is consistent with our model: as the probe wavelength tunes, different pairs of phase-matched PhP frequencies are selected, but their difference frequency—the synthesized beat—remains approximately constant due to

the similar dispersion slopes. This demonstrates that the synthesized beat frequency can be designed by choosing appropriate experimental conditions, and the platform supports continuous tunability across a range of frequencies, offering flexibility for tailored waveform generation.

Active control of coherent PhP interference

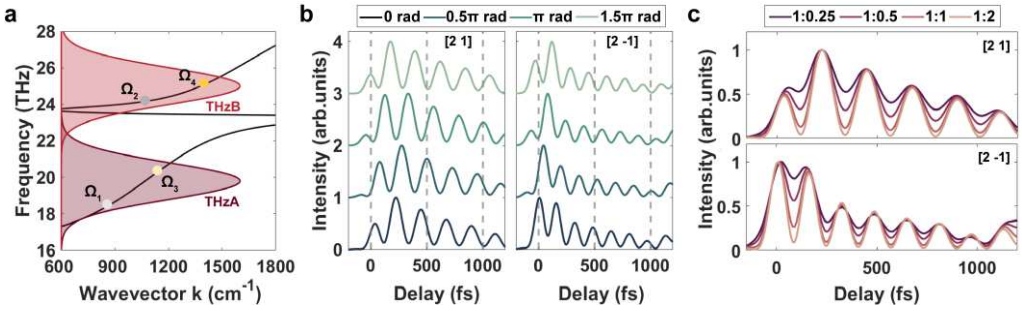


Fig. 5. **Double-pulse coherent excitation for multi-parameter manipulation of phonon polariton time-domain waveforms. a** Double THz narrowband pulses. The black line corresponds to the PhP dispersion curve, while the Ω represents the phase-matched PhPs frequencies. The color-shaded regions represent THz spectra. **b** Phase-dependent manipulation of the FWM waveform, achieved by tuning the CEP of one pulse and fixing the other. Different colors represent the variation of CEP of THzA. The dashed line is a guide to the eye. **c** Intensity-dependent control of the modulation depth, where the color scale represents the field intensity ratio between the two THz pulses. The legend represents the amplitude ratio of THzA to THzB, with the amplitude of THzA fixed.

To actively manipulate the oscillation waveform, a double-THz-pulse excitation scheme is implemented. Specifically, the original single broadband, intense THz pulse is spectrally separated into two narrowband pulses (denoted as THzA and THzB), whose central frequencies are tuned near the phase-matched PhPs frequencies (Fig. 5a). This mode-selective excitation enables independent addressing of the two PhP components while preserving their coherence.

Two complementary control parameters are demonstrated: First, varying the CEP of one pulse while holding the other fixed provides deterministic control over the phase of the time-domain oscillation, enabling waveform shaping (e.g., sine-to-cosine conversion) without

altering the beat frequency or modulation depth (Fig. 5b). This establishes the CEP as a pure phase knob for editing the temporal profile of the synthesized waveform. Second, varying the field strength of one pulse while keeping the other fixed changes the interference term $|C_1||C_2|$, thereby controlling the modulation depth independently of the waveform shape and beat frequency (Fig. 5c). This demonstrates amplitude as an independent control parameter.

It should be noted that theoretically, the double-THz-pulse scheme enables continuous tunability of both the amplitude and phase of the FWM waveform. However, in practical applications, the modulation precision of this scheme must be considered. Taking waveform (phase) control as an example (see Supplementary Note 6 for detailed analysis), the resolution of the FWM modulation signal is primarily limited by two factors: the step resolution of the delay stage and the energy stability of the experimental system. Currently, the minimum step of the servo motor used in the experiment is typically 0.1 μm, corresponding to a modulation signal resolution of approximately 3.1 fs. Meanwhile, measurements show that the laser system's energy stability is about 5% (RMS), corresponding to a time resolution of approximately 1.9 fs for the modulation signal. Therefore, under the current experimental configuration, the resolution of the double-THz-pulse scheme is mainly limited by the step precision of the delay stage. More importantly, by further optimizing the energy stability of the laser system and employing motors with higher step precision, it is even possible to achieve signal modulation with sub-femtosecond ($\leqslant$1 fs) time resolution.

Taken together, these results achieve decoupled, multi-parameter control over the synthesized coherent state: frequency (set by phase matching), phase (controlled by CEP), and amplitude (controlled by field strength) can be independently programmed. This transforms the system from a passive beat-note observer to an active, programmable terahertz waveform synthesizer.

Discussion

In conclusion, this work establishes a paradigm-shifting framework for terahertz photonics: a programmable, all-optical waveform synthesizer that generates coherent virtual beat notes decoupled from material eigenmodes. Using phase-matching-directed four-wave mixing in α-quartz, we actively synthesize beat frequencies of 4.3/6.0 THz and 6.3/7.1 THz—frequencies that are not native to the material but emerge as the difference between two phase-matched PhPs. Through a double-THz-pulse excitation scheme, we achieve independent control over the temporal waveform (via carrier-envelope phase) and modulation depth (via field strength) while keeping the beat frequency constant, demonstrating decoupled multi-parameter manipulation of the synthesized coherent state. This work not only demonstrates a new capability in α-quartz but also establishes a universal framework for all-optical engineering of coherent terahertz waveforms, with profound implications for future terahertz photonic devices and ultrafast science.

Materials and methods

Experiments

This study utilized an *x*-cut (5.0×5.0×0.1 mm³) α-SiO_2 single crystal, which belongs to the space group $P3_221$ and is a uniaxial dielectric with strong, resonantly enhanced $\chi^{(3)}$ nonlinearity in the THz range[42,43]. At room temperature, it possesses a total of $\Gamma_{\mathrm{opt}} = 4A_1 + 4A_2 + 8E$ optical modes, among which the A_1 modes are Raman-active, the A_2 phonons are infrared-active, and the E modes are both infrared- and Raman-active[44]. As shown in Fig. 1a, the experiment employed a transmission-geometry pump-probe system. The pump pulses were generated by a home-built frequency-tunable intense mid-to-far-infrared source[45], with a central frequency range of 20–40 THz and a maximum field strength reaching up to 20 MV/cm. The probe pulse was the output from a 1 kHz repetition rate optical parametric amplifier. The pump and probe beams were co-focused onto the sample using an off-axis parabolic mirror

with a drilled hole. The pump polarization was aligned either parallel or perpendicular to the crystal's optical axis, corresponding to the ΓA and ΓM directions in reciprocal space, respectively. The probe polarization was fixed along the optical axis. Since the optical axis is a high-symmetry direction, the second-order nonlinear effects dominated by $\chi^{(2)}$ vanish[46]. The transmitted signal was measured by a spectrometer. A metal wire-grid polarizer was placed in front of the spectrometer to extract signals with specific polarizations. The data error is primarily limited by the spectrometer resolution and the data acquisition length.

Phase-matching between probe pulse and phonon-polariton

The dispersion curve equation for phonon polariton is given by[44,47]:

$$\varepsilon(\omega) = \frac{c^2 k^2}{\omega^2} = \varepsilon_\infty + \sum \frac{\Omega_{\mathrm{TO-j}}^2 S_{\mathrm{TO-j}}}{\Omega_{\mathrm{TO-j}}^2 - \omega^2 - i\gamma_{\mathrm{j}}\omega} \tag{5}$$

where ε_∞ is the high-frequency dielectric constant, $\Omega_{\mathrm{TO-j}}$ represents the frequency of the infrared-active transverse optical phonon, $S_{\mathrm{TO-j}}$ is the oscillator coupling strength, and $\gamma_{\mathrm{TO-j}}$ is the damping constant of the oscillator. Specific parameters can be found in Supplementary Table S1. The phase-matching conditions for the FWM process between the forward/backward propagating phonon polariton wave vector $k_\pm$ and the NIR probe pulse are as follows:

$$k_\pm = \frac{1}{c}[2\omega_{\mathrm{NIR}}(n_{\mathrm{f}} - n_{\mathrm{NIR}}) \pm \omega_{\mathrm{PhP}} n_{\mathrm{f}}] \tag{6}$$

here, c is the speed of light in vacuum, ω_{NIR} and ω_{PhP} denote the frequencies corresponding to the incident fundamental NIR photon and the FWM photon generated by matching the phonon polariton, respectively, while n_{NIR} and n_{f} represent the refractive indices corresponding to the incident fundamental photon and the FWM photon. The different combinations of $k_\pm$ and $\pm\omega_{\mathrm{PhP}}$ constitute four propagation scenarios.

Finite-Difference Time-Domain Simulation

The FDTD method is a direct time-domain numerical approach for solving Maxwell's curl equations[24,48]. In one dimension, this method is significantly simplified and is well-suited for studying the propagation, reflection, and transmission of plane waves in layered media or structures with translational invariance. Its core lies in the discretization of the spatial coordinate (assumed as the z-axis) and the temporal coordinate, employing Yee's staggered grid scheme: the electric field component E_{y} is defined at integer grid points i, while the orthogonal magnetic field component H_{x} is defined at half-integer grid points i+1/2. In the time domain, the sampling points for E_{y} and H_{x} are also staggered by half a time step. This arrangement naturally converts the spatial derivative $\partial/\partial z$ in Maxwell's equations into a central-difference format and the temporal derivative $\partial/\partial t$ into a leapfrog iteration scheme, thereby forming a complete set of explicit update algorithms.

To reduce numerical errors in the calculations, the computed magnetic field H_{x} and electric field E_{y} need to be renormalized as follows:

$$H_{\mathrm{x}}^{*} = \eta_0 H_{\mathrm{x}}, \eta_0 = \sqrt{\frac{\mu_0}{\epsilon_0}} \tag{7}$$

Since we need to account for the material's refractive index dispersion in both the THz and infrared frequency ranges, Maxwell's equations in the 1D case become:

$$\frac{\partial E_{\mathrm{y}}}{\partial t} = -\frac{\mu_{\mathrm{r}}^{\mathrm{xx}}}{c}\frac{\partial H_{\mathrm{x}}^{*}}{\partial z} \tag{8}$$

$$\frac{\partial H_{\mathrm{x}}^{*}}{\partial t} = \eta_0 \frac{\partial D_{\mathrm{y}}}{\partial z} \tag{9}$$

$$D_{\mathrm{y}} = \epsilon_0 \varepsilon_{\infty} E_{\mathrm{y}} + P_{\mathrm{y}} \tag{10}$$

Dispersion is introduced by considering the polarization P_{y}. For linear dispersion:

$$\frac{\partial P_{\mathrm{y}}}{\partial t} = J_{\mathrm{y}} \tag{11}$$

$$\frac{\partial J_{\mathrm{y}}}{\partial t} + \gamma J_{\mathrm{y}} + \Omega^2 P_{\mathrm{y}} = \epsilon_0 \Omega^2 S E_{\mathrm{y}} \tag{12}$$

These equations describe the dispersion given by the Lorentz model, where γ is the damping coefficient, Ω is the resonant frequency, ϵ_0 is the vacuum permittivity, and S is the oscillator strength. For multiple oscillators, multiple polarization terms are considered accordingly. For nonlinear effects, primarily the nonlinear response of the IR probe pulse is considered in a similar manner. In this case, the driving force for the oscillator is the second- or third-order nonlinear driving term. For the FWM process:

$$\frac{\partial P_{\mathrm{y-NIR}}^{\mathrm{NL}}}{\partial t} = J_{\mathrm{y-NIR}}^{\mathrm{NL}} \tag{13}$$

$$\frac{\partial J_{\mathrm{y-NIR}}^{\mathrm{NL}}}{\partial t} + \gamma J_{\mathrm{y-NIR}}^{\mathrm{NL}} + \Omega^2 P_{\mathrm{y-NIR}}^{\mathrm{NL}} = \epsilon_0 \Omega^2 \chi_{\mathrm{ir}}^{(3)} E_{\mathrm{y-NIR}} E_{\mathrm{y-NIR}} E_{\mathrm{y-PhP}} \tag{14}$$

By discretizing Eq. (2-4) and (7-10) and performing numerical solutions, the phenomena of dispersion and nonlinear interactions occurring during pulse wave propagation in the material can be accurately obtained. It is noteworthy that in FDTD simulations, the phase-matching effect is automatically included, which is a key distinction from frequency-domain simulations. In the simulation process, the second-order nonlinear coefficient of the material is set to zero, and only the FWM phenomenon resulting from third-order nonlinear effects is considered. It should be noted that although small discrepancies (e.g., in the temporal waveform evolution) exist between the FDTD simulation results and the experiment, due to the influence of various parameters such as phonon frequency, damping coefficient, sample thickness and boundary condition selection, the simulation fully reproduces the phase matching of PhPs and the "beat frequency" oscillatory phenomenon. Therefore, these minor differences can be disregarded.

Acknowledgements

This work was supported by National Key Research and Development Program of China (2022YFA1604400); National Natural Science Foundation of China (12325409, 12388102, 12304374, U23A6002, 12404400); Shanghai Natural Science Foundation (23ZR1471600); Shanghai Pilot Program for Basic Research, Chinese Academy of Sciences, Shanghai Branch;

CAS Project for Young Scientists in Basic Research (YSBR-059, YSBR-127); China Postdoctoral Science Foundation(2025M773338).

Author contributions

J.G. conducted the experimental measurements. J.H. and Y. F. constructed the theoretical model and conceived the simulation. J.G. and Y.F. wrote the manuscript. Y.T. and L.S. conceived and planned the project. All authors discussed the results and contributed to the manuscript revisions.

Data availability

All data supporting the main findings of this work are available from the corresponding author upon reasonable request.

Conflict of interest

The authors declare no competing interests.

References

1 Huang, K. On the Interaction between the Radiation Field and Ionic Crystals. *Proc. R. Soc. Lond. A Math. Phys. Sci.* **208**, 352-365 (1951).

2 Bakker, H. J., Hunsche, S. & Kurz, H. Coherent phonon polaritons as probes of anharmonic phonons in ferroelectrics. *Rev. Mod. Phys.* **70**, 523-536 (1998).

3 Basov, D. N., Fogler, M. M. & García de Abajo, F. J. Polaritons in van der Waals materials. *Science* **354**, aag1992 (2016).

4 Foteinopoulou, S. *et al.* Phonon-polaritonics: enabling powerful capabilities for infrared photonics. *Nanophotonics* **8**, 2129-2175 (2019).

5 Henstridge, M. *et al.* Nonlocal nonlinear phononics. *Nat. Phys.* **18**, 457-461 (2022).

6 Wu, Y. *et al.* Manipulating polaritons at the extreme scale in van der Waals materials. *Nat. Rev. Phys.* **4**, 578-594 (2022).

7 Galiffi, E. *et al.* Extreme light confinement and control in low-symmetry phonon-polaritonic crystals. *Nat. Rev. Mater.* **9**, 9-28 (2024).

8 Kowalski, R. A. *et al.* Ultraconfined terahertz phonon polaritons in hafnium dichalcogenides. *Nat. Mater.* **24**, 1735-1741 (2025).

9 Barra-Burillo, M. *et al.* Microcavity phonon polaritons from the weak to the ultrastrong phonon–photon coupling regime. *Nat. Commun.* **12**, 6206 (2021).

10 Guo, Q. *et al.* Hyperbolic phonon-polariton electroluminescence in 2D heterostructures. *Nature* **639**, 915-921 (2025).

11 He, P. *et al.* Strongly confined mid-infrared to terahertz phonon polaritons in ultrathin $SrTiO_3$. *Sci. Adv.* **11**, eady7316 (2025).

12 Fang, Y. *et al.* Coherent manipulation of second-harmonic generation via terahertz-field mediated phonon-polariton in zinc oxide. *Nat. Commun.* **16**, 5598 (2025).

13 Pei, Y. *et al.* Low-dimensional heat conduction in surface phonon polariton waveguide. *Nat. Commun.* **14**, 8242 (2023).

14 Meng, Y. *et al.* Photonic van der Waals integration from 2D materials to 3D nanomembranes. *Nat. Rev. Mater.* **8**, 498-517 (2023).

15 Iyikanat, F., Konečná, A. & García de Abajo, F. J. Nonlinear tunable vibrational response in hexagonal boron nitride. *ACS Nano* **15**, 13415-13426 (2021).

16 Ginsberg, J. S. *et al.* Phonon-enhanced nonlinearities in hexagonal boron nitride. *Nat. Commun.* **14**, 7685 (2023).

17 Giles, A. J. *et al.* Ultralow-loss polaritons in isotopically pure boron nitride. *Nat. Mater.* **17**, 134-139 (2018).

18 Folland, T. G. *et al.* Reconfigurable infrared hyperbolic metasurfaces using phase change materials. *Nat. Commun.* **9**, 4371 (2018).

19 Aghamiri, N. A. *et al.* Reconfigurable hyperbolic polaritonics with correlated oxide metasurfaces. *Nat. Commun.* **13**, 4511 (2022).

20 Hu, H. *et al.* Doping-driven topological polaritons in graphene/α-MoO_3 heterostructures. *Nat. Nanotechnol.* **17**, 940-946 (2022).

21 He, M. *et al.* Polariton design and modulation via van der Waals/doped semiconductor heterostructures. *Nat. Commun.* **14**, 7965 (2023).

22 Kampfrath, T., Tanaka, K. & Nelson, K. A. Resonant and nonresonant control over matter and light by intense terahertz transients. *Nat. Photonics* **7**, 680-690 (2013).

23 Mankowsky, R., Först, M. & Cavalleri, A. Non-equilibrium control of complex solids by nonlinear phononics. *Rep. Prog. Phys.* **79**, 064503 (2016).

24 von Hoegen, A. *et al.* Probing the interatomic potential of solids with strong-field nonlinear phononics. *Nature* **555**, 79-82 (2018).

25 Li, X. *et al.* Terahertz field–induced ferroelectricity in quantum paraelectric $SrTiO_3$. *Science* **364**, 1079-1082 (2019).

26 Nova, T. F., Disa, A. S., Fechner, M. & Cavalleri, A. Metastable ferroelectricity in optically strained $SrTiO_3$. *Science* **364**, 1075-1079 (2019).

27 Yang, J. *et al.* Manipulating terahertz phonon-polariton in the ultrastrong coupling regime with bound states in the continuum. *Light Sci. Appl* **14**, 360 (2025).

28 Xu, J. *et al.* Dynamic tuning of Bloch modes in anisotropic phonon polaritonic crystals. *Light Sci. Appl* **15**, 41 (2026).

29 Martín-Sánchez, J. *et al.* Focusing of in-plane hyperbolic polaritons in van der Waals crystals with tailored infrared nanoantennas. *Sci. Adv.* **7**, eabj0127 (2021).

30 Huang, Y. *et al.* Giant Kerr nonlinearity of terahertz waves mediated by stimulated phonon polaritons in a microcavity chip. *Light Sci. Appl* **13**, 212 (2024).

31 Białek, M. *et al.* Hybridization of terahertz phonons and magnons in disparate and spatially-separated material specimens. *Adv. Funct. Mater.* **35**, 2416037 (2025).

32 Lu, Y. *et al.* Giant enhancement of THz-frequency optical nonlinearity by phonon polariton in ionic crystals. *Nat. Commun.* **12**, 3183 (2021).

33 Bakker, H. J., Hunsche, S. & Kurz, H. Observation of THz phonon-polariton beats in $LiTaO_3$. *Phys. Rev. Lett.* **69**, 2823-2826 (1992).

34 Bakker, H. J., Hunsche, S. & Kurz, H. Investigation of anharmonic lattice vibrations with coherent phonon polaritons. *Phys. Rev. B* **50**, 914-920 (1994).

35 Goldshteyn, J. *et al.* Selective preparation and detection of phonon polariton wavepackets by stimulated Raman scattering. *Phys. Status Solidi B* **251**, 821-828 (2014).

36 Hioki, T., Hashimoto, Y. & Saitoh, E. Coherent oscillation between phonons and magnons. *Commun. Phys.* **5**, 115 (2022).

37 Sivarajah, P. *et al.* THz-frequency magnon-phonon-polaritons in the collective strong-coupling regime. *J. Appl. Phys.* **125**, 213103 (2019).

38 Subedi, A., Cavalleri, A. & Georges, A. Theory of nonlinear phononics for coherent light control of solids. *Phys. Rev. B* **89**, 220301 (2014).

39 Subedi, A. Proposal for ultrafast switching of ferroelectrics using midinfrared pulses. *Phys. Rev. B* **92**, 214303 (2015).

40 Disa, A. S., Nova, T. F. & Cavalleri, A. Engineering crystal structures with light. *Nat. Phys.* **17**, 1087-1092 (2021).

41 Först, M. *et al.* Nonlinear phononics as an ultrafast route to lattice control. *Nat. Phys.* **7**, 854-856 (2011).

42 Zibod, S. *et al.* Strong Nonlinear Response in Crystalline Quartz at THz Frequencies. *Adv. Opt. Mater.* **11**, 2202343 (2023).

43 Zhou, B. *et al.* Measurement of the Dispersion of $\chi^{(3)}$ of SiO_2 and SiN Across the THz and Far-Infrared Frequency Bands. *Laser Photonics Rev.* **18**, 2301321 (2024).

44 He, M. *et al.* Fundamental infrared absorption features of α-quartz: An unpolarized single-crystal absorption infrared spectroscopic study. *Vib. Spectrosc.* **101**, 52-63 (2019).

45 Sang, J. *et al.* Hybrid optical parametric amplifier for few-cycle infrared and terahertz pulses generation. *Opt. Laser Technol.* **184**, 112573 (2025).

46 Boyd, R. W. *Nonlinear Optics, Third Edition*. (Academic Press, Inc., 2008).

47 Spitzer, W. G. & Kleinman, D. A. Infrared Lattice Bands of Quartz. *Phy. Rev.* **121**, 1324-1335 (1961).

48 Taflove, A. & Hagness, S. *Computational Electrodynamics: The Finite-Difference Time-Domain Method, 3rd edition*. Vol. 2062 (2005).

Supplementary Files

This is a list of supplementary files associated with this preprint. Click to download.

- Supplementaryinformation1.docx